Element Specific Atom Counting at the Atomic Scale by Combining HAADF STEM and EDX

*Annick De Backer Zezhong Zhang Karel H.W. van den Bos Eva Bladt Ana Sánchez-Iglesias Luis M. Liz-Marzán Peter D. Nellist Sara Bals Sandra Van Aert**

Dr. A. De Backer, Dr. Z. Zhang, Dr. K.H.W. van den Bos, Dr. E. Bladt, Prof. Dr. S. Bals, Prof. Dr. S. Van Aert
EMAT, University of Antwerp, Groenenborgerlaan 171, 2020 Antwerp, Belgium
NANOlab Center of Excellence, University of Antwerp, Belgium
Email Address: sandra.vanaert@uantwerpen.be

Dr. A. Sánchez-Iglesias
CIC biomaGUNE, Basque Research and Technology Alliance (BRTA), 20014, Donostia-San Sebastián, Spain
Centro de Investigación Biomédica en Red de Bioingeniería, Biomateriales y Nanomedicina (CIBER-BBN), 20014, Donostia-San Sebastián, Spain

Prof. Dr. L.M. Liz-Marzán
CIC biomaGUNE, Basque Research and Technology Alliance (BRTA), 20014, Donostia-San Sebastián, Spain
Centro de Investigación Biomédica en Red de Bioingeniería, Biomateriales y Nanomedicina (CIBER-BBN), 20014, Donostia-San Sebastián, Spain
Ikerbasque, Basque Foundation for Science, 48009 Bilbao, Spain

Prof. Dr. P.D. Nellist
Department of Materials, University of Oxford, Parks Road, OX1 3PH Oxford, United Kingdom

Keywords: *quantitative electron microscopy, energy dispersive X-ray spectroscopy, scanning transmission electron microscopy, statistical parameter estimation theory, bimetallic nanoparticles, atom-counting*

A new methodology is presented to count the number of atoms in multimetallic nanocrystals by combining energy dispersive X-ray spectroscopy (EDX) and high angle annular dark field scanning transmission electron microscopy (HAADF STEM). For this purpose, the existence of a linear relationship between the incoherent HAADF STEM and EDX images is exploited. Next to the number of atoms for each element in the atomic columns, the method also allows quantification of the error in the obtained number of atoms, which is of importance given the noisy nature of the acquired EDX signals. Using experimental images of an Au@Ag core-shell nanorod, it is demonstrated that 3D structural information can be extracted at the atomic scale. Furthermore, simulated data of a Au@Pt core-shell nanorod show the prospect to characterize heterogeneous nanostructures with adjacent atomic numbers.

1 Introduction

Multimetallic nanocrystals are of great scientific and technological interest because of their unique electronic, optical, or catalytic properties, which are often superior in comparison to their monometallic counterparts [1, 2, 3, 4]. These properties are largely determined by the atomic structure and composition of the nanocrystal [5]. High angle annular dark field (HAADF) scanning transmission electron microscopy (STEM) provides images with sub-Ångström resolution in which intensities scale with both thickness and composition [6, 7]. For monometallic nanocrystals, it has been shown that counting the number of atoms from HAADF STEM images can be of great value in determining the exact arrangement of all atoms in three dimensions (3D) [8, 9, 10, 11, 12, 13, 14, 15]. For heterogeneous structures, however, the presence of so-called Z-contrast complicates this procedure, since the different elements and their exact 3D arrangement in each atomic column will contribute differently to the image intensity [16, 17, 18, 19]. Therefore, we developed a new methodology, which combines HAADF STEM imaging and elemental mapping by energy dispersive X-ray (EDX) spectroscopy with atomic resolution [20, 21, 22, 23, 24]. This method offers new opportunities to count the number of atoms corresponding to each specific element, even when the difference in atomic number is only one.

It was previously shown that, by calibrating experimental HAADF STEM images with respect to the number of incident electrons [25, 26, 27, 28], one can count the number of atoms in a given atomic column when directly comparing the calibrated experimental image intensities with simulated intensities as a function of thickness [8, 14]. Hereby, one uses so-called scattering cross-sections, i.e. the total intensity of electrons scattered by a single column. This measure is robust for imaging parameters including e.g. defocus and source size broadening, and increases monotonically with thickness for homogeneous materials [8, 9, 14, 13, 29, 30]. To facilitate atom-counting for heterogeneous structures, we introduced the atomic lensing model, which provides scattering cross-sections of mixed columns much faster than time-consuming image simulations [16]. Still, prior knowledge about the overall shape and thickness of the nanostructure is mostly required since the scattering cross-section values of different mixed columns overlap in the presence of noise. Therefore, it has been suggested to record HAADF STEM images with different detector settings [19, 31]. However, the detection of compositional differences in HAADF STEM becomes increasingly more challenging, or even impossible, when the difference between the atomic numbers of the elements decreases. Alternatively, elemental maps can be acquired using EDX spectroscopy. Nowadays, detector systems are available that enable even atomically resolved EDX maps [32, 33, 34]. By including ionization potentials into simulations [22, 35], one can quantify the EDX images on an absolute scale after normalizing with respect to the number of incident electrons. This normalization is, however, challenging because factors such as detector efficiency and geometry should be accurately measured [33, 36, 37, 38, 39, 40]. More recently, it was suggested to count atoms by matching scattering cross-sections to library values obtained from experimental images of single element wedge-shaped particles [41, 42, 43] . This, however, limits the applicability of atom-counting from EDX maps since such samples are not available for every element. To overcome this limitation, we exploit the existence of a linear scaling between EDX and HAADF scattering cross-sections. Using this linear scaling, a novel methodology is proposed which combines EDX and HAADF STEM images to count the number of atoms without requiring any EDX calibration standards. This method will be applied to an experimental dataset from an Ag-coated Au nanorod, and the prospects of the method are additionally illustrated for the analysis of nanostructures with adjacent atomic numbers, based on simulated data for a Pt-coated Au nanorod.

2 Methods

2.1 Linear scaling between HAADF STEM and EDX scattering cross-sections

Theory:
Both HAADF STEM and EDX imaging are incoherent techniques. In HAADF STEM imaging, the recorded electrons mainly arise from thermal diffuse scattering (TDS) [44, 45]. In the so-called absorptive potential approximation, appropriate for thinner samples [46, 47], the image intensity from the jth slice of the specimen is then described by the overlap between the electron density of the STEM probe and a high-angle TDS absorptive potential of the specimen $V^{HA}_{TDS}(\mathbf{x})$ [48, 49, 50, 51]:

$$\begin{aligned} &I_j^{HAADF}(\mathbf{x}_0) \\ &\quad = \int \left|\Psi_j^{STEM}(\mathbf{x},\mathbf{x}_0)\right|^2 \left[1-\exp\left(-\frac{2}{\hbar\nu}V^{HA}_{j,TDS}(\mathbf{x})\right)\right] d\mathbf{x} \qquad (1) \\ &\approx \frac{2}{\hbar\nu}\int \left|\Psi_j^{STEM}(\mathbf{x},\mathbf{x}_0)\right|^2 V^{HA}_{j,TDS}(\mathbf{x}) d\mathbf{x}, \qquad (2) \end{aligned}$$

where $\mathbf{x} = (x, y)$ is a 2D real space coordinate vector, $\mathbf{x}_0 = (x_0, y_0)$ is the electron probe position, $\Psi^{STEM}(\mathbf{x}, \mathbf{x}_0)$ is the electron wave function, and ν is the speed of the electron. The total HAADF STEM intensity from all J slices is then obtained by summing the intensity of each slice. Similarly, the generation of X-rays, and therefore the recorded EDX signal, may be described by the overlap of the

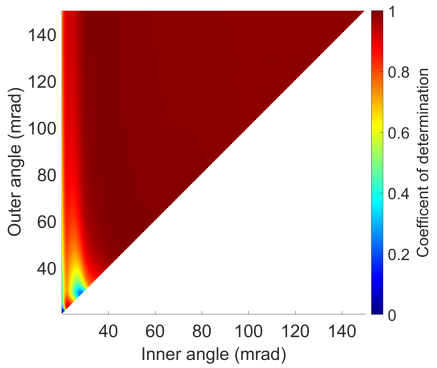

Figure 1: Coefficient of determination (R^2-value) of the ADF-EDX linear dependence for a range of different inner and outer collection angles for an Au crystal.

probe electron density and a projected effective ionization potential $V_{eff}^{EDX}(\mathbf{x})$ [52, 22, 53, 54, 55]:

$$I_j^{EDX}(\mathbf{x}_0) = \frac{2}{\hbar\nu}\int \left|\Psi_j^{STEM}(\mathbf{x},\mathbf{x}_0)\right|^2 V_{j,eff}^{EDX}(\mathbf{x})d\mathbf{x}. \tag{3}$$

Here, it is assumed that absorption of X-rays within the specimen is small and can be neglected, which is reasonable for thin specimens [56]. Since the distributions of the TDS absorptive and effective ionization potential are similar [57, 35], a linear relationship between the recorded image intensities in HAADF STEM imaging and EDX spectroscopy is expected. The same linear relationship will exist for the scattering cross-sections (SCS), corresponding to the total intensity of electrons scattered by a single atomic column. In practice, these SCSs can be measured using statistical parameter estimation theory, either by estimating the volume of a Gaussian peak that models the shape of the atomic column [58, 59] or by integrating intensities over the probe positions in the vicinity of a single column of atoms [29]. This linear relationship indicates that, also in EDX STEM imaging, the scattering cross-section increases monotonically with thickness and can thus be used to count the number of atoms in a column.

Simulations:
Since the equations in the previous sections involve some approximations, they are only valid for a high inner angle of the annular STEM detector and thin specimens. Therefore, the linear relationship has been further investigated using full frozen phonon multislice simulations for EDX and ADF STEM signals. Results of this extensive study have been discussed by Zhang et al. [60]. This study revealed that ADF and EDX signals have a linear dependence if the signals are fully incoherent. To illustrate this relation, ADF and EDX scattering cross-sections were simulated for all possible inner and outer collection angles for an Au crystal in a [001] orientation with varying thickness (1-25 atoms), using an acceleration voltage of 300 keV, a probe convergence semi-angle of 20 mrad, and no lens aberrations. The ADF scattering cross-sections as a function of the EDX scattering cross-sections are fitted with a linear model and the goodness of fit was determined by the coefficient of determination or so-called R^2-value. A perfect linear relationship results in an R^2 value equal to 1. **Figure 1** shows the R^2-values as a function of the inner and outer detector angles. If the inner angle is larger than 40 mrad, then for this set of microscope settings, i.e. the specific values for voltage and convergence angle used in the simulation, a linear dependence can be expected between the ADF and EDX scattering cross-sections. The linear relationship between both types of signals suggests that EDX STEM scattering cross-sections can indeed be used for atom-counting.

Experiment:
Since the amount of experimentally detected X-rays is determined by the exact detector geometry, efficiency, solid angle, and holder shadowing, it is important to confirm this relationship experimentally for our instrument. For this purpose, experimental HAADF STEM and EDX images of a CeO_2 nanoparticle were recorded (see **Figure. 2**(a)-(c)). The scattering cross-sections were estimated from the HAADF STEM image, by means of the StatSTEM software [59], where the image is modeled as a superposition

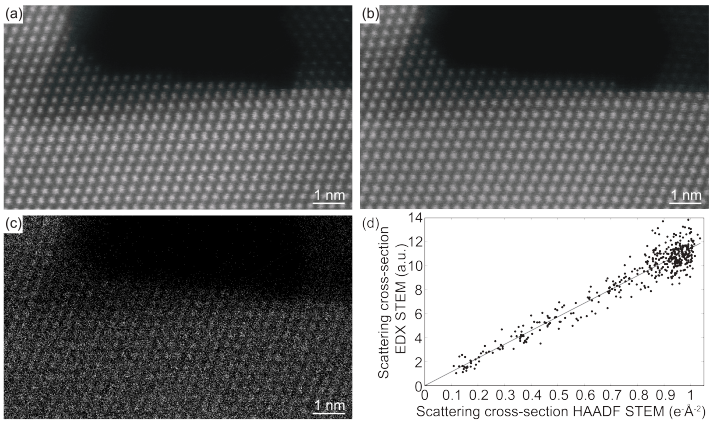

Figure 2: Experimental HAADF STEM images of a CeO_2 nanoparticle (a) before and (b) after EDX mapping. (c) Experimental atomic resolution EDX elemental map for the Ce L shell. (d) The EDX STEM scattering cross-sections as a function of the HAADF STEM scattering cross-sections. The gray line is shown to highlight the linear relationship between the scattering cross-sections of both techniques.

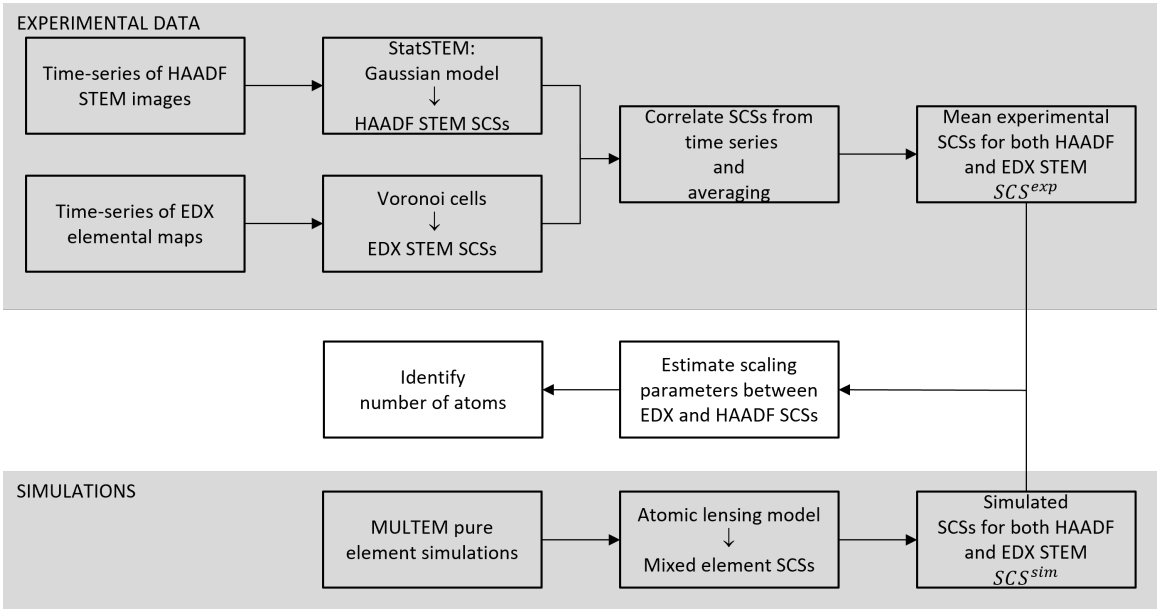

Figure 3: Schematic of the method to count the number of atoms of each type, based on HAADF and EDX images.

of Gaussian peaks. The HAADF STEM scattering cross-section equals the volume under the estimated Gaussian peak. Due to the lower signal-to-noise (SNR) ratio in the EDX STEM image, here the Gaussian peaks are modeled using the estimated atomic column positions from the corresponding HAADF STEM image. Even though CeO_2 is relatively beam-stable, an HAADF STEM image is acquired before and after EDX mapping to confirm the absence of intolerable structural changes. The mean scattering cross-sections of the two HAADF STEM images are compared to the EDX scattering cross-sections on a column-by-column basis, as shown in Figure 2(d). The results confirm the linear relationship between both techniques highlighted by the fitted gray line. Deviations from this gray line can be explained by the relatively low SNR in the EDX STEM image. In addition to the demonstration of the linear relationship between the HAADF STEM and EDX scattering cross-sections from theory and simulations in the previous paragraphs, this relationship is hereby also confirmed based on a set of experimental scattering cross-sections, validating the hypothesis that EDX STEM scattering cross-sections can be used for atom-counting.

2.2 Estimating the scaling parameters between HAADF STEM and EDX scattering cross-sections

The atom-counting methodology for heterogeneous nanocrystals by combining HAADF STEM and EDX is based on a comparison of experimentally measured scattering cross-section values and simulated scattering cross-section values. For this purpose, the experimental HAADF STEM images are normalized with respect to the incident beam using the method described by Rosenauer et al. [27], enabling one to directly compare experimentally measured cross-sections to simulated values. For EDX imaging, the proven linear relationship between the scattering cross-sections of the EDX and HAADF signals can be utilized to simulate the EDX scattering cross-section values. For this purpose, scaling parameters are required for the multiple element types. Since these specimen dependent constants are altered by microscope parameters, such as detector geometry and efficiency [36, 37, 38, 39, 40], a new quantitative framework is proposed to estimate the scaling parameters iteratively. In this manner, the estimation of the number of atoms is independent of the exact detector geometry, efficiency, fixed angle, and holder shadowing of the experimental set-up. The methodology, in which we combine the EDX and HAADF STEM scattering cross-sections, will be explained for structures containing two types of elements but can be extended to multiple elements. A schematic of the method is shown in **Figure 3**.

Typically, due to the long acquisition time used during EDX imaging, a time-series of EDX and HAADF-STEM images can be acquired. From these images, the scattering cross-sections are measured using the well-established statistical parameter estimation framework implemented in StatSTEM [30], as described in Section 2.1. Due to the low SNR in the individual EDX STEM images, the scattering cross-sections in the EDX images are measured using Voronoi cells. With this approach, each pixel is assigned to the nearest atomic column, with the positions of the atomic columns being determined from the simultaneously recorded HAADF STEM images. To mutually correlate the coordinates of the atomic columns in each time-series image, the drift between consecutive images is determined. Details on this correlation procedure are described in the Supporting Information. In this manner, mean scattering cross-sections with their corresponding errors are determined for each atomic column over the time-series.

The monotonic increase of the scattering cross-sections with thickness can now be used to count the number of atoms from both the HAADF and EDX STEM images. At this point, measured scattering cross-sections are matched to simulated library values. The library values for the HAADF STEM scattering cross-sections of the mixed atomic columns are generated using frozen lattice image simulations of the pure element crystals [61, 62] in combination with the atomic lensing model [16]. Debye-Waller factors are selected using the parametrization of Gao and Peng [63]. As demonstrated by Zhang et al. [60], the atomic lensing model can also be used to predict EDX scattering cross-sections.

The main challenge is to estimate the two scaling parameters for the EDX cross-sections of the two types of elements. It is assumed that the experimental HAADF scattering cross-section requires no scaling with respect to simulation [26, 27, 13]. For a single atomic column, because of the unknown EDX scaling parameters, there is an ambiguity between sample thickness and composition. It is, however, possible to determine an upper and lower bound to the thickness from the HAADF scattering cross-section by assuming the column is either entirely the lighter or heavier species respectively. For each possible thickness, only one column composition can then match the HAADF scattering cross-section, allowing the EDX scaling parameters then to be determined for that composition. By repeating this for all possible thicknesses compatible with the HAADF scattering cross-section, it becomes clear that a finite range of possible EDX scaling parameters for that single column is possible. For a sample with variations in thickness and composition, different columns will lead to different possible ranges of scaling parameters. With sufficient atomic columns in an experiment, the scaling parameters that are most compatible with all of the columns can be determined.

For a practical method to estimate the normalization constants for the different elements determining the scaling relation between the EDX and HAADF STEM scattering cross-sections, we combine the experimental and simulated scattering cross-sections of both types of signals (EDX + HAADF) in one framework. In this procedure, the weighted sum of squared differences between the experimentally

measured mean scattering cross-sections SCS^{exp} and the simulated scattering cross-sections SCS^{sim} from the different signals is minimized:

$$(\hat{a}_2, \hat{a}_3) = \arg\min_{a_2,a_3} \sum_{n=1}^{N} \sum_{k=1}^{3} \frac{1}{\sigma_{k,n}^2} \left(a_k \cdot SCS_{k,n}^{\text{sim}} - SCS_{k,n}^{\text{exp}}\right)^2 . \quad (4)$$

In this expression, n is the atomic column index, N equals the total number of atomic columns and k indicates the different signals. We set $k = 1$ for the HAADF STEM signal, and $k = 2$ and $k = 3$ for the EDX measurements of two different elements. The scaling parameters, or normalization constants, are denoted by a_k, where $a_1 = 1$ for the HAADF STEM measurements. In this manner, only a_2 and a_3 are estimated for the scaling of the two different elements. Furthermore, $SCS_{k,n}^{\text{sim}}$ and $SCS_{k,n}^{\text{exp}}$ denote the simulated and experimental scattering cross-section value of column n for signal k, respectively. The weights can be chosen equal to the inverse of the variance of the measured mean scattering cross-section values $\sigma_{k,n}^2$, since the measured EDX and HAADF scattering cross-section observations are not equally reliable. Indeed, the SNR in the EDX images is relatively low as compared to the HAADF STEM images and the error on the mean scattering cross-sections is therefore higher for the EDX measurements. This knowledge is incorporated into the estimation algorithm via the weights.

The scaling parameters a_2 and a_3 are estimated in an iterative framework. For each iteration, i.e. for the intermediate values of the scaling parameters before convergence is reached, the best matching composition and thickness for each atomic column are determined by the minimized weighted squared differences between the library values and the normalized EDX and HAADF STEM scattering cross-sections. A limited thickness range and a limited set of compositions can be evaluated as discussed above. In the analyses that follow in Sections 3.1 and 3.2, core-shell structures are studied, reducing the possible atom orderings to be assumed. Nevertheless, the change in scattering cross-section due to a different ordering of the atoms within an atomic column is small and can only be detected at very high doses [64]. Therefore, assuming a specific ordering will not affect the assigned number of atoms in each atomic column at the typically used incident electron doses.

Having found the best-fit thickness and composition for all available columns given the current estimation of the scaling parameters, the refinement of the scaling parameters is performed by applying a derivative-free unconstrained non-linear optimization method, the Nelder-Mead simplex method [65], to Equation(4). Once the scaling parameters are estimated, the number of atoms per element in each atomic column is identified.

In the next Section, the method will be applied to Ag@Au and Pt@Au bimetallic nanoparticles. However, the method will also be applicable to other systems such as core-shell semiconductor nanostructures and materials containing light elements. In case the X-ray energies of different elements in a heterogeneous nanostructure are critically overlapping, reliable elemental maps cannot be obtained and therefore the method cannot be used to unscramble the number of atoms in those cases. Nevertheless, modern instrumentation has an excellent energy resolution ($< 140\ eV$) which allows distinguishing e.g. Au and Pt spectra [66, 67]. If elemental maps with enough detected X-rays are available, the key point to apply the method is the linear relationship between the EDX and HAADF scatering cross-section values. If this requirement is fulfilled, which will be more easily for lighter elements, then reliable atom-counting results can be expected.

3 Results

3.1 Proof of concept experiment on an Ag@Au nanorod

The method to count atoms in heterogeneous nanocrystals using EDX STEM imaging is applied to experimental EDX and HAADF STEM images of an Au@Ag core-shell nanorod. A total acquisition time of 60 minutes was applied to collect a significant EDX signal, using a beam current of approximately 50 pA. Individual EDX maps were acquired every 5 minutes, followed by the acquisition of a HAADF STEM image. Using this procedure, possible beam damage can be tracked during the acquisition of the

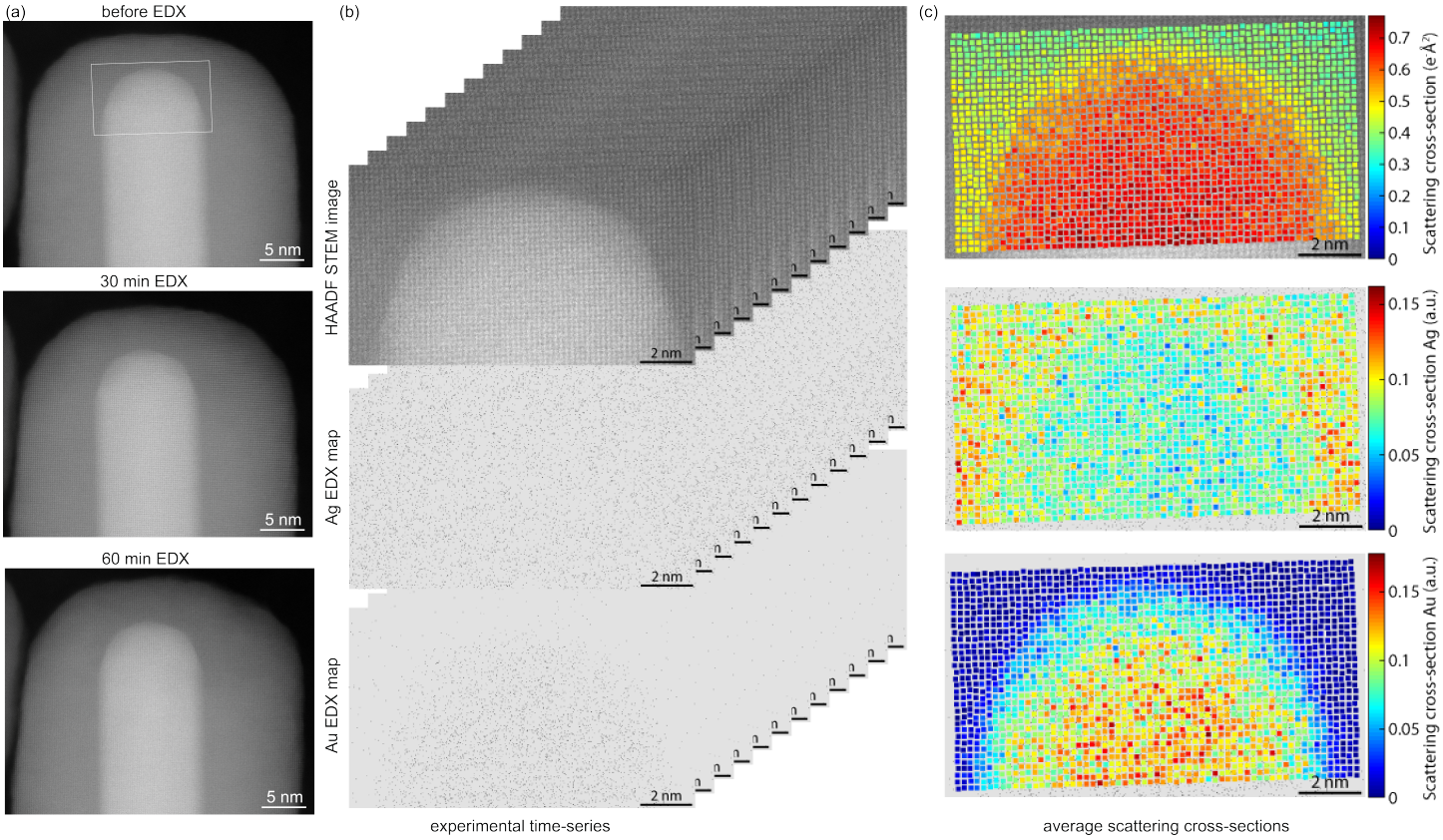

Figure 4: (a) Experimental HAADF STEM images of an Au@Ag core-shell nanorod recorded before, after 30 minutes, and after 60 minutes of EDX mapping. The nanorod remains sufficiently stable over time. (b) Experimental time-series of HAADF STEM and EDX elemental maps. (c) Measured average scattering cross-section values from HAADF STEM images and EDX elemental maps for Ag and Au.

images. To reduce the acquisition time, this procedure was applied to a selected part of the Au@Ag core-shell nanorod where mixed atomic columns are observed, as indicated in **Figure 4**(a). The HAADF STEM images in Figure 4(a) indicate that the particle remains sufficiently stable under the electron beam. The experimental time-series for HAADF STEM imaging and the corresponding Ag and Au EDX maps are shown in Figure 4(b). The average scattering cross-section values measured from the maps are presented in Figure 4(c). The atom-counting results obtained using the methodology described in section 2.2 are presented in **Figure 5**. The method was applied to the atomic columns located inside the white rectangle in Figure 5, for which the EDX signal was recorded. Outside this rectangular region, Ag atoms are counted using only HAADF STEM imaging, since it can be observed from the HAADF STEM contrast that this region only contains the Ag shell. The counting results for both types of elements agree well with the expected results for a symmetrical Au@Ag core-shell nanorod, based on the contrast of the HAADF STEM images. It should be noticed here that, in contrast to the approach of van den Bos et al. [16], we do not exploit any prior knowledge about the shape or thickness of the structure.
To further investigate the accuracy and precision of the obtained atom-counting results using our novel algorithm, we also determined the root mean squared error (RMSE) on the atom-counting results inside the rectangular region of Figure 5. The RMSE could be obtained using noise realizations of empirical simulations. Details of the empirical simulations for the RMSE analysis are described in the Supporting Information. The average error on the number of atoms in a column and the error on the total number of atoms are summarized in **Table 1**. The RMSE is a bit larger for the lighter Ag atoms as compared to the RMSE for the Au atoms or the total number of atoms. The RMSE for each atomic column is visualized in **Figure S2** together with the number of atoms for each column. From this figure, also the spatial distribution of the RMSE can be studied and it is clear that the error is larger for the mixed columns containing atoms from both the Au core and the Ag shell. For the atomic columns containing only Ag shell atoms, the error is significantly smaller in the analyzed region as compared to the error of the pure

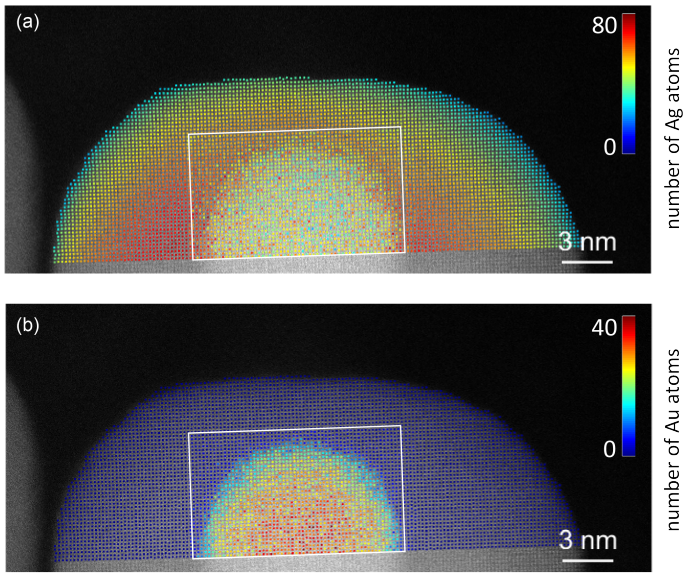

Figure 5: Number of (a) Ag and (b) Au atoms, shown as an overlay on the experimental HAADF STEM images of an Au@Ag core-shell nanorod. The white square indicates the region where Ag and Au atoms are counted by combining EDX and HAADF STEM imaging.

type	**total** number of atoms ± error	average error in a **column**
Ag	(114 037 ± 691) atoms	± 5.6 atoms
Au	(37 083 ± 339) atoms	± 2.5 atoms
total number of atoms (Ag+Au)	(151 120 ± 370) atoms	± 3.2 atoms

Table 1: Summary of the RMSE on the total number of atoms and the average error on the estimated number of atoms in a column for Ag, Au, and the total number of atoms for the Au@Ag core-shell nanorod.

Ag columns. Given the highly noisy nature of the EDX signals and the total number of atoms in the atomic columns going up to more than 80 atoms, the obtained errors are more than acceptable.

3.2 Exploring possibilities through a simulated Au@Pt nanorod

In the experimental study, the large difference in atomic number between Ag and Au enables one to also extract information to identify the number of Ag and Au atoms from HAADF STEM images only, assuming some prior knowledge about the shape of the particle [16]. This becomes impossible when elements with similar atomic numbers are present. Especially for these materials, the new framework offers new opportunities to count atoms since EDX spectroscopy allows one to record images element-wise. To illustrate this, HAADF STEM images and EDX maps of an Au@Pt core-shell nanorod were simulated. The simulated HAADF STEM image and corresponding Pt and Au EDX elemental maps are shown in **Figure 6**. The simulated core-shell structure is relaxed by molecular dynamics simulations employing the embedded atom method potential [68] using the LAMMPS open source code [69] and contains 1370 Pt atoms and 281 Au atoms. The image simulations were performed using the muSTEM package [47] along the [001] orientation. An acceleration voltage of 300 kV, a semi-convergence angle of 20 mrad, a Debye-Waller factor corresponding to 290 K, a pixel size of 0.2454 Å and no aberrations were chosen. The HAADF detector ranges from 50 to 150 mrad and averaging over 30 unique phonon configurations was performed. For the EDX signals the 2p orbitals of Pt and Au were used to create the elemental maps. Libraries for the pure element columns were simulated under the same conditions for a [001] Pt and Au FCC crystal.
First, the methodology was applied to the infinite dose simulations. The ground truth number of atoms, estimated number of atoms, and difference maps (ground truth - estimated) are also presented in Figure 6. The observed differences in the atom-counting results are directly related to the unavoidable small mismatch between the simulated library of scattering cross-sections assuming the bulk unit cell and the

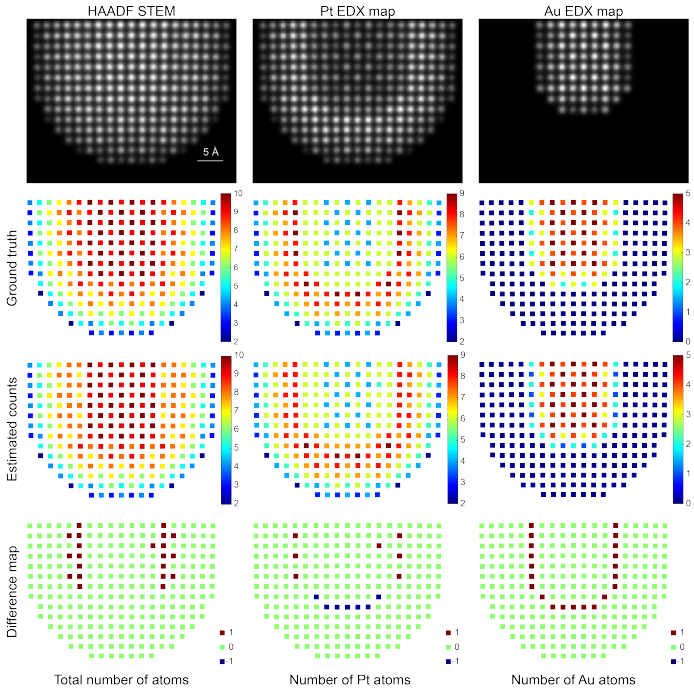

Figure 6: Simulated HAADF STEM image and EDX elemental maps of an Au@Pt core-shell nanorod, together with the ground truth atom-counts, the estimated atom-counts, and the difference maps for the total number of atoms and both the number of Pt and Au atoms in an atomic column.

measured scattering cross-sections from the relaxed Pt-Au nanorod. The difference maps obtained for the simulation of the Au@Pt nanorod using the unrelaxed structure do not reveal any miscounted number of atoms in the columns (see **Figure S3**).
Next, the simulation set-up is made similar to an experimental set-up corresponding to EDX mapping of 60 minutes where the results are stored every 5 minutes followed by the acquisition of a HAADF STEM image. For this purpose a time series of 12 images is generated. After that, Poisson noise (50 noise realizations) is included in the simulated HAADF STEM image and the EDX elemental maps in order to evaluate the effect of a limited incident electron dose on the obtained counting results. For the HAADF STEM image an incident electron dose of $5 \cdot 10^4$ e$^-$Å^{-2} per frame is used and for the EDX elemental maps $5 \cdot 10^6$ e$^-$Å^{-2}. In order to get some extra insight in the atom-counting errors for the different elements and the total number of atoms, the collection efficiency of the EDX signal was varied from 100% to 1%. An example of such a simulated dataset is shown in **Figure S4**(a), for a collection efficiency of 5%. For the set of simulations as a function of the collection efficiency, the average RMSE for the number of atoms in the column was evaluated. The result is presented in **Figure 7**. The angular efficiency of our SuperX system is $0.7Sr/(4\pi)$, which is about 5%. In that case, the average error is less than one atom. The RMSE per atomic column for 5% efficiency is also shown in Figure S4(b). From this figure, it can be observed that the RMSE reaches values up to 3 for the number of Pt and Au atoms in the mixed atomic columns, but is less on average. However, shadowing from the holder can block up to 50% of the EDX signal, reducing the collection efficiency further to 2.5%. In that case the error on the atom-counting results would increase significantly. From Figure 7, we can also extract the expected RMSE when changing the electron dose for the acquisition of the EDX signal. For example, when doubling the incident electron dose, the RMSE will correspond to the value shown at the double collection efficiency. However, since the EDX experiments are already very dose-consuming, increasing the electron dose is unfavorable because we want to avoid as much as possible beam damage. This RMSE analysis indicates, that if we act with great caution during the experimental acquisition, reliable counting results can be obtained for the different types of elements. On the other hand, it also reveals that, with the current collection efficiency, we are at a turning point for a trustworthy quantification of the EDX signals at the atomic level in terms of e.g. number of atoms. The introduction of new instruments with an angular

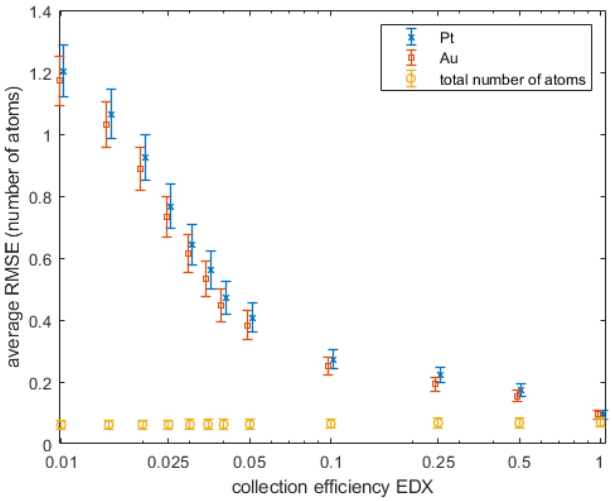

Figure 7: Average RMSE per atomic column as a function of the collection efficiency of the EDX signal for counting the number of Pt, Au, and total atoms for the PtAu nanorod.

efficiency towards $4Sr/(4\pi) \sim 30\%$ [70, 67] will greatly benefit quantification at the atomic level. This new type of detector will also bring new capabilities to study more beam-sensitive nanostructures, such as light element structures, for which limiting the incident electron dose during imaging is essential.

4 Conclusion

In summary, we have introduced a new method to unambiguously count atoms in heterogeneous nanocrystals. Here the linear relationship between the scattering cross-sections in EDX and HAADF STEM imaging enables us to combine theses techniques. By applying this approach successfully to experimental images of Au@Ag and simulated Au@Pt core-shell nanorods, we have demonstrated that it enables one to retrieve the number of atoms of each element. With noise realizations of (empirical) simulations, we could also quantify the RMSE on the estimated number of atoms for the 2 types of elements and the total number of atoms. Given the noisy nature of the EDX signals, the obtained errors are remarkably tolerable in order to quantify nanostructures at the atomic scale. Considering that this novel methodology can be applied even when elements have almost identical atomic numbers, it opens up new opportunities to reveal the 3D structure atom-by-atom for a wide variety of multimetallic nanocrystals.

5 Experimental Section

Au@Ag nanoparticle synthesis:
Chemicals: Gold (III) chloride trihydrate ($HAuCl_4$, $\geq$ 99%), hexadecyltrimethylammonium bromide (CTAB, $\geq$ 99%), benzyldimethylhexadecylammonium chloride (BDAC, 99%), sodium borohydride ($NaBH_4$, $\geq$ 98%), silver nitrate ($AgNO_3$, $\geq$ 99%), hydrochloric acid (HCl, 37%) and ascorbic acid (AA, $\geq$ 99%) were purchased from Sigma-Aldrich. All reactants were used without further purification. Milli-Q water (resistivity 18.2 MΩ· cm at 25°C) was used in all experiments. All glassware was washed with aqua regia, rinsed with Milli-Q water, and dried before use.
Synthesis of gold nanorods [71]: Gold nanorods were prepared using Ag-assisted seeded growth. Seeds were prepared by reduction of $HAuCl_4$ (0.25 mM, 5 mL) with freshly prepared $NaBH_4$ (10 mM, 0.3 mL) in aqueous CTAB solution (100 mM). An aliquot of seed solution (0.5 mL) was added to a growth solution (250 mL) containing CTAB (100 mM), $HAuCl_4$ (0.5 mM), ascorbic acid (0.8 mM), $AgNO_3$ (0.12 mM), and HCl (19 mM). The mixture was left undisturbed at 30°C for 2 h. The solution was centrifuged twice (8000 rpm, 30 min) to remove excess silver salt, ascorbic acid, CTAB and HCl,

and redispersed in BDAC 10 mM.
Silver-coated gold nanorods[72]: To a dispersion of gold nanorods (10 mL) containing BDAC (10 mM) and metallic gold (0.25 mM) at 60°C, were added solutions of $AgNO_3$ (0.25 mL, 10 mM) and AA (0.1 mL, 100 mM) under vigorous stirring. The mixture was stirring at 60°C for 4 h. Finally, the obtained solution was centrifuged and redispersed in water.

EDX and HAADF STEM imaging:
The experimental EDX and HAADF STEM images have been recorded at a probe-corrected Thermo Fisher Scientific Titan^3 equipped with a SuperX system, operated at 300 keV. The HAADF STEM regime hs been selected using a probe convergence semi-angle of 20 mrad and a STEM detector with collection angles ranging from 46 to 215 mrad. For CeO_2, the EDX image, yielding atomic resolution, is obtained by mapping for 17 minutes with a beam current of approximately 170 pA. For the Au@Ag nanorod, a total acquisition time of 60 minutes is applied using a beam current of approximately 50 pA. More details on the experimental data acquisition are described in the Supporting Information.

Supporting Information
Supporting Information is available from the Wiley Online Library or from the author.

Acknowledgments
This work was supported by the European Research Council (Grant 770887 PICOMETRICS to S.V.A., Grant 815128 REALNANO to S.B., and Grant 823717 ESTEEM3). The authors acknowledge financial support from the Research Foundation Flanders (FWO, Belgium) through project fundings (G.0267.18N, G.0502.18N, G.0346.21N) and a postdoctoral grant to A.D.B.

Conflict of Interest
The authors declare no conflict of interest.

Data Availability Statement
The data that support the findings of this study are available from the corresponding author upon reasonable request.

References

[1] A. Henglein, *Journal of Physical Chemistry B* **2000**, *104* 2201.

[2] H. Ataee-Esfahani, L. Wang, Y. Nemoto, Y. Yamauchi, *Chemistry of Materials* **2010**, *22*, 23 6310.

[3] S. Gómez-Graña, J. Pérez-Juste, R. A. Alvarez-Puebla, A. Guerrero-Martínez, L. M. Liz-Marzán, *Advanced Optical Materials* **2013**, *1*, 7 477.

[4] Y. Zhang, X. Li, K. Li, B. Xue, C. Zhang, C. Du, Z. Wu, W. Chen, *ACS applied materials & interfaces* **2017**, *9*, 38 32688.

[5] A. Zaleska-Medynska, M. Marchelek, M. Diak, E. Grabowska, *Advances in colloid and interface science* **2016**, *229* 80.

[6] P. E. Batson, N. Dellby, O. L. Krivanek, *Nature* **2002**, *418* 617.

[7] R. Erni, M. D. Rossell, C. Kisielowski, U. Dahmen, *Physical Review Letters* **2009**, *102* 096101.

[8] J. M. LeBeau, S. D. Findlay, L. J. Allen, S. Stemmer, *Nano Letters* **2010**, *10* 4405.

[9] S. Van Aert, K. J. Batenburg, M. D. Rossell, R. Erni, G. Van Tendeloo, *Nature* **2011**, *470* 374.

[10] S. Bals, M. Casavola, M. A. van Huis, S. Van Aert, K. J. Batenburg, G. Van Tendeloo, D. Vanmaekelbergh, *Nano Letters* **2011**, *11*, 8 3420.

[11] S. Bals, S. Van Aert, C. P. Romero, K. Lauwaet, M. J. Van Bael, B. Schoeters, B. Partoens, E. Yücelen, P. Lievens, G. Van Tendeloo, *Nature Communications* **2012**, *3* 897.

[12] A. De Backer, G. T. Martinez, A. Rosenauer, S. Van Aert, *Ultramicroscopy* **2013**, *134* 23.

[13] S. Van Aert, A. De Backer, G. T. Martinez, B. Goris, S. Bals, G. Van Tendeloo, *Physical Review B* **2013**, *87* 064107.

[14] L. Jones, K. E. MacArthur, V. T. Fauske, A. T. J. van Helvoort, P. D. Nellist, *Nano Letters* **2014**, *14*, 11 6336.

[15] A. De Backer, L. Jones, I. Lobato, T. Altantzis, B. Goris, P. D. Nellist, S. Bals, S. Van Aert, *Nanoscale* **2017**, *9* 8791.

[16] K. H. W. van den Bos, A. De Backer, G. T. Martinez, N. Winckelmans, S. Bals, P. D. Nellist, S. Van Aert, *Physical Review Letters* **2016**, *116* 246101, accepted.

[17] G. T. Martinez, A. Rosenauer, A. De Backer, J. Verbeeck, S. Van Aert, *Ultramicroscopy* **2014**, *137* 12.

[18] R. Ishikawa, A. R. Lupini, S. D. Findlay, T. Taniguchi, S. J. Pennycook, *Nano Letters* **2014**, *14* 1903.

[19] J. Y. Zhang, J. Hwang, B. J. Isaac, S. Stemmer, *Scientific Reports* **2015**, *5* 12419.

[20] A. J. D'Alfonso, B. Freitag, D. Klenov, L. J. Allen, *Physical Review B* **2010**, *81* 100101(R).

[21] M.-W. Chu, S. C. Liou, C.-P. Chang, F.-S. Choa, C. H. Chen, *Physical Review Letters* **2010**, *104*, 19 196101.

[22] L. J. Allen, A. J. D'Alfonso, B. Freitag, D. O. Klenov, *MRS Bulletin* **2012**, *37* 47.

[23] P. Lu, R. Yuan, J. M. Zuo, *Microscopy and Microanalysis* **2017**, *23*, 1 145.

[24] C. Arias-Duque, E. Bladt, M. A. Muñoz, J. C. Hernández-Garrido, M. A. Cauqui, J. M. Rodríguez-Izquierdo, G. Blanco, S. Bals, J. J. Calvino, J. A. Pérez-Omil, M. P. Yeste, *Chemistry of Materials* **2017**, *29*, 21 9340.

[25] L. D. Menard, S.-P. Gao, H. Xu, R. D. Twesten, A. S. Harper, Y. Song, G. Wang, A. D. Douglas, J. C. Yang, A. I. Frenkel, R. G. Nuzzo, R. W. Murray, *The Journal of Physical Chemistry B* **2006**, *110*, 26 12874.

[26] J. M. LeBeau, S. Stemmer, *Ultramicroscopy* **2008**, *108* 1653.

[27] A. Rosenauer, K. Gries, K. Müller, A. Pretorius, M. Schowalter, A. Avramescu, K. Engl, S. Lutgen, *Ultramicroscopy* **2009**, *109* 1171.

[28] G. T. Martinez, L. Jones, A. De Backer, A. Béché, J. Verbeeck, S. Van Aert, P. D. Nellist, *Ultramicroscopy* **2015**, *159* 46, submitted.

[29] H. E, K. E. MacArthur, T. J. Pennycook, E. Okunishi, A. J. D'Alfonso, N. R. Lugg, L. J. Allen, P. D. Nellist, *Ultramicroscopy* **2013**, *133* 109.

[30] A. De Backer, A. De wael, J. Gonnissen, S. Van Aert, *Ultramicroscopy* **2015**, *151* 46.

[31] K. Müller-Caspary, O. Oppermann, T. Grieb, F. F. Krause, A. Rosenauer, M. Schowalter, T. Mehrtens, A. Beyer, K. Volz, P. Potapov, *Scientific Reports* **2016**, *6* 37146.

[32] A. Genc, L. Kovarik, M. Gu, H. Cheng, P. Plachinda, L. Pullan, B. Freitag, C. Wang, *Ultramicroscopy* **2013**, *131* 24.

[33] G. Kothleitner, M. J. Neish, N. R. Lugg, S. D. Findlay, W. Grogger, F. Hofer, L. J. Allen, *Physical Review Letters* **2014**, *112* 085501.

[34] B. Goris, L. Polavarapu, S. Bals, G. Van Tendeloo, L. M. Liz-Marzán, *Nano letters* **2014**, *14*, 6 3220.

[35] M. P. Oxley, L. J. Allen, *Acta Crystallographica* **2000**, *A56*.

[36] M. Watanabe, D. B. Williams, *Journal of Microscopy* **2006**, *221*, 2 89.

[37] C. Doshi, G. van Riessen, E. Balaur, M. D. de Jonge, A. G. Peele, *Ultramicroscopy* **2015**, *148* 20.

[38] Z. Chen, A. J. D'Alfonso, M. Weyland, D. J. Taplin, L. J. Allen, S. D. Findlay, *Ultramicroscopy* **2015**, *157* 21.

[39] T. J. A. Slater, A. Janssen, P. H. C. Camargo, M. Grace Burke, N. J. Zaluzec, S. J. Haigh, *Ultramicroscopy* **2016**, *162* 61.

[40] W. Xu, J. H. Dycus, J. M. LeBeau, *Ultramicroscopy* **2016**, *164* 51.

[41] K. E. MacArthur, T. J. A. Slater, S. J. Haigh, D. Ozkaya, P. D. Nellist, S. Lozano-Perez, *Materials Science and Technology* **2016**, *32* 248.

[42] K. E. MacArthur, T. J. A. Slater, S. J. Haigh, D. Ozkaya, P. D. Nellist, S. Lozano-Perez, *Microscopy and Microanalysis* **2016**, *22*, 01 71.

[43] A. Varambhia, L. Jones, A. London, D. Ozkaya, P. D. Nellist, S. Lozano-Perez, *Micron* **2018**, *113* 69.

[44] P. Hartel, D. Rose, C. Dinges, *Ultramicroscopy* **1996**, *63* 63.

[45] P. D. Nellist, S. J. Pennycook, *Advances in Imaging and Electron Physics* **2000**, *113* 147.

[46] J. M. LeBeau, S. D. Findlay, L. J. Allen, S. Stemmer, *Physical Review Letters* **2008**, *100* 206101.

[47] L. J. Allen, A. J. D'Alfonso, S. D. Findlay, *Ultramicroscopy* **2015**, *151* 11.

[48] L. J. Allen, C. J. Rossouw, *Phys. Rev. B* **1990**, *42* 11644.

[49] A. Weickenmeier, H. Kohl, *Acta Crystallographica Section A* **1991**, *47*, 5 590.

[50] K. Ishizuka, *Ultramicroscopy* **2002**, *90* 71.

[51] A. Rosenauer, M. Schowalter, J. T. Titantah, D. Lamoen, *Ultramicroscopy* **2008**, *108*, 12 1504.

[52] L. J. Allen, S. D. Findlay, M. P. Oxley, C. J. Rossouw, *Ultramicroscopy* **2003**, *96* 47.

[53] C. Dwyer, volume 175 of *Advances in Imaging and Electron Physics*, 145–199. Elsevier, **2013**.

[54] N. R. Lugg, G. Kothleitner, N. Shibata, Y. Ikuhara, *Ultramicroscopy* **2015**, *151* 150.

[55] Z. Chen, D. J. Taplin, M. Weyland, L. J. Allen, S. D. Findlay, *Ultramicroscopy* **2017**, *176* 52.

[56] S. J. Pennycook, P. D. Nellist, chapter 2, 108. Springer, **2011**.

[57] L. J. Allen, T. W. Josefsson, *Physical Review B* **1995**, *52*, 5 3184.

[58] S. Van Aert, J. Verbeeck, R. Erni, S. Bals, M. Luysberg, D. Van Dyck, G. Van Tendeloo, *Ultramicroscopy* **2009**, *109* 1236.

[59] A. De Backer, K. H. W. van den Bos, W. Van den Broek, J. Sijbers, S. Van Aert, *Ultramicroscopy* **2016**, *171* 104.

[60] Z. Zhang, I. Lobato, A. De Backer, S. Van Aert, P. D. Nellist, *Ultramicroscopy* **2022**, – .

[61] I. Lobato, D. Van Dyck, *Ultramicroscopy* **2015**, *156* 9.

[62] I. Lobato, S. Van Aert, J. Verbeeck, *Ultramicroscopy* **2016**, *168* 17.

[63] H. X. Gao, L.-M. Peng, *Acta Crystallographica A* **1999**, *55* 926.

[64] K. H. W. van den Bos, L. Janssens, A. De Backer, P. D. Nellist, S. Van Aert, *Ultramicroscopy* **2019**.

[65] J. C. Lagarias, J. A. Reeds, M. H. Wright, P. E. Wright, *SIAM Journal of Optimization* **1998**, *9*, 1 112.

[66] A. Pedrazo-Tardajos, E. Arsalan Irmak, V. Kumar, A. Sánchez-Iglesias, Q. Chen, M. Wirix, B. Freitag, W. Albrecht, S. Van Aert, L. M. Liz-Marzán, S. Bals **2022**, *16* 9608.

[67] N. Zaluzec *27* 2070.

[68] C. J. O?Brien, C. M. Barr, P. M. Price, K. Hattar, S. M. Foiles, *Journal of Materials Science* **2017**, *53*, 4.

[69] A. P. Thompson, H. M. Aktulga, R. Berger, D. S. Bolintineanu, W. M. Brown, P. S. Crozier, P. J. in 't Veld, A. Kohlmeyer, S. G. Moore, T. D. Nguyen, R. Shan, M. J. Stevens, J. Tranchida, C. Trott, S. J. Plimpton, *Computer Physics Communications* **2022**, *271* 108171.

[70] URL `https://www.thermofisher.com/be/en/home/electron-microscopy/products/transmission-electron-microscopes/spectra-ultra-tem.html?cid=fl-spectra-ultra`.

[71] M. Liu, P. Guyot-Sionnest, *Journal of Physical Chemistry B* **2005**, *109* 22192.

[72] S. Gómez-Graña, B. Goris, T. Altantzis, C. Fernández-López, E. Carbó-Argibay, A. Guerrero-Martínez, N. Almora-Barrios, N. López, S. Pastoriza-Santos, J. Pérez-Juste, S. Bals, G. Van Tendeloo, L. M. Liz-Marzán, *Journal of Physical Chemistry Letters* **2013**, *4* 2209.

Supporting Information
Element Specific Atom Counting at the Atomic Scale by Combining HAADF STEM and EDX

*Annick De Backer Zezhong Zhang Karel H.W. van den Bos Eva Bladt Ana Sánchez-Iglesias Luis M. Liz-Marzán Peter D. Nellist Sara Bals Sandra Van Aert**

Dr. A. De Backer, Dr. Z. Zhang, Dr. K.H.W. van den Bos, Dr. E. Bladt, Prof. Dr. S. Bals, Prof. Dr. S. Van Aert
EMAT, University of Antwerp, Groenenborgerlaan 171, 2020 Antwerp, Belgium
NANOlab Center of Excellence, University of Antwerp, Belgium
Email Address: sandra.vanaert@uantwerpen.be

Dr. A. Sánchez-Iglesias
CIC biomaGUNE, Basque Research and Technology Alliance (BRTA), 20014, Donostia-San Sebastián, Spain
Centro de Investigación Biomédica en Red de Bioingeniería, Biomateriales y Nanomedicina (CIBER-BBN), 20014, Donostia-San Sebastián, Spain

Prof. Dr. L.M. Liz-Marzán
CIC biomaGUNE, Basque Research and Technology Alliance (BRTA), 20014, Donostia-San Sebastián, Spain
Centro de Investigación Biomédica en Red de Bioingeniería, Biomateriales y Nanomedicina (CIBER-BBN), 20014, Donostia-San Sebastián, Spain
Ikerbasque, Basque Foundation for Science, 48009 Bilbao, Spain

Prof. Dr. P.D. Nellist
Department of Materials, University of Oxford, Parks Road, OX1 3PH Oxford, United Kingdom

1 Data acquisition

Fast scanning multi-frame EDX-ADF STEM imaging is proven to be effective in suppressing beam damage [1]. Therefore, a time series of EDX and HAADF STEM images is acquired. For a reliable analysis of the EDX signals, the total EDX counts should be high enough to obtain a sufficient signal-to-noise ratio in the EDX elemental maps. Due to the small EDX scattering cross-sections and the limited collection efficiency of the detector, we need a sufficiently long acquisition time to accumulate enough counts. Though it may vary for different elements and microscope settings, a good rule of thumb for a signal-to-noise ratio of 5 with a detector efficiency of 2.5%, is to use a total electron dose at the order of $10^7 - 10^8$ $e^-/Å^2$. For the Au@Ag nanorod, the total acquisition time was 60 minutes, using a beam current of 50 pA and scanning area of 14.3×15.1 $Å^2$. Note that only a rectangular area of this scanning area has been used for atom-counting in the mixed atomic columns. The EDX spectrum imaging results are stored every five minutes, followed by the acquisition of a calibrated HAADF STEM image. In this manner, the HAADF STEM images can be used to track any undesirable effects during the acquisition, such as e.g. high drift, beam induced tilt, contamination, and damage of the specimen. On the other hand, these atomic resolution HAADF STEM images serve as an input to correlate the time-series of HAADF STEM images and the corresponding EDX elemental maps. It is important to note that the recent simultaneous ADF-EDX multi-frame capability in modern acquisition software facilitates this correction process.

2 Correlating time-series images

The relation between the coordinates of the atomic columns in the images of the time-series is found by describing the drift between the consecutive images as an affine transformation **T**, including horizontal shear α_s, vertical scaling β_s, and shift in the $x-$ and $y-$direction x_s and y_s:

$$\mathbf{T}\left(\begin{bmatrix} x \\ y \end{bmatrix}\right) = \begin{bmatrix} 1 & \alpha_s \\ 0 & \beta_s \end{bmatrix} \begin{bmatrix} x \\ y \end{bmatrix} + \begin{bmatrix} x_s \\ y_s \end{bmatrix}. \tag{1}$$

Here, x and y is the coordinate set to which the affine transformation is applied. The affine transformation **T** is found by minimising the squared difference between the pixel intensities of consecutive images. In this manner, the atomic columns in consecutive images can be correlated.

3 Empirical simulation of EDX and HAADF STEM scattering cross-sections for RMSE analysis

A set of empirically simulated scattering cross-sections for both EDX and HAADF STEM can be computed using the estimated scaling parameters and estimated number of atoms determined from the experimental Ag-coated Au nanorod. The procedure that is followed is schematically shown in **Figure 1**(a). For each atomic column with a specific composition and containing a specific number of atoms derived from the experiment, a value for the HAADF STEM scattering cross-section can be obtained using the simulated scattering cross-sections for the mixed columns. Based on the estimated scaling parameters for Ag and Au, a set of EDX scattering cross-sections can also be obtained for both types of elements. For the composition we assume here a symmetrical core-shell particle. In order to create a dataset which replicates the experimental conditions, the noise-free set of scattering cross-sections is duplicated 12 times to mimic the 12 images of the time-series. Next, 50 noise realisations of the dataset are generated. As a first step, Poisson noise is included using the experimental incident electron dose for the HAADF STEM images ($3.6 \cdot 10^4$ e$^-$Å^{-2} per frame). Additionally, the effect of scan distortions is included in the simulation of the scattering cross-sections. Based on a previous study, this scan distortion is modelled as a normal distribution with a variance of $4.5 \cdot 10^{-4}\mu_g$, with μ_g the average scattering cross-section of an atomic column with g atoms [2]. For the EDX scattering cross-sections, Poisson noise can be directly applied to the scaled simulated scattering cross-sections values. Indeed, the simulated scattering cross-section values multiplied with the estimated scaling factors include the effect of the experimental incident electron dose used for EDX imaging. In Figure 1(b), a set of empirically simulated scattering cross-sections is plotted as a function of the number of atoms in the column. The variability in this scatter plot is comparable with the variability in the scatter plot of the experimentally measured set of scattering cross-sections values. The excellent agreement for both the EDX as well as the HAADF STEM scattering cross-sections supports the validity of this empirical approach.
For each noise realisation, the scattering cross-sections are then averaged over the empirically simulated time-series to get mean values together with a measure for their precision. In the following step, the empirically simulated scattering cross-sections are matched to the simulated values assuming a linear scaling between the STEM and EDX scattering cross-sections using the iterative weighted least squares minimisation described in the methodology. From the 50 sets of estimated number of atoms from the different noise realisations, the root mean squared error can be determined.

References

[1] L. Jones, A. Varambhia, R. Beanland, D. Kepaptsoglou, I. Griffiths, A. Ishizuka, F. Azough, R. Freer, K. Ishizuka, D. Cherns, Q. M. Ramasse, S. Lozano-Perez, P. D. Nellist **2018**, *67* i98.

[2] S. Van Aert, A. De Backer, L. Jones, G. T. Martinez, A. Béché, P. D. Nellist, *Physical Review Letters* **2019**, *122* 066101.

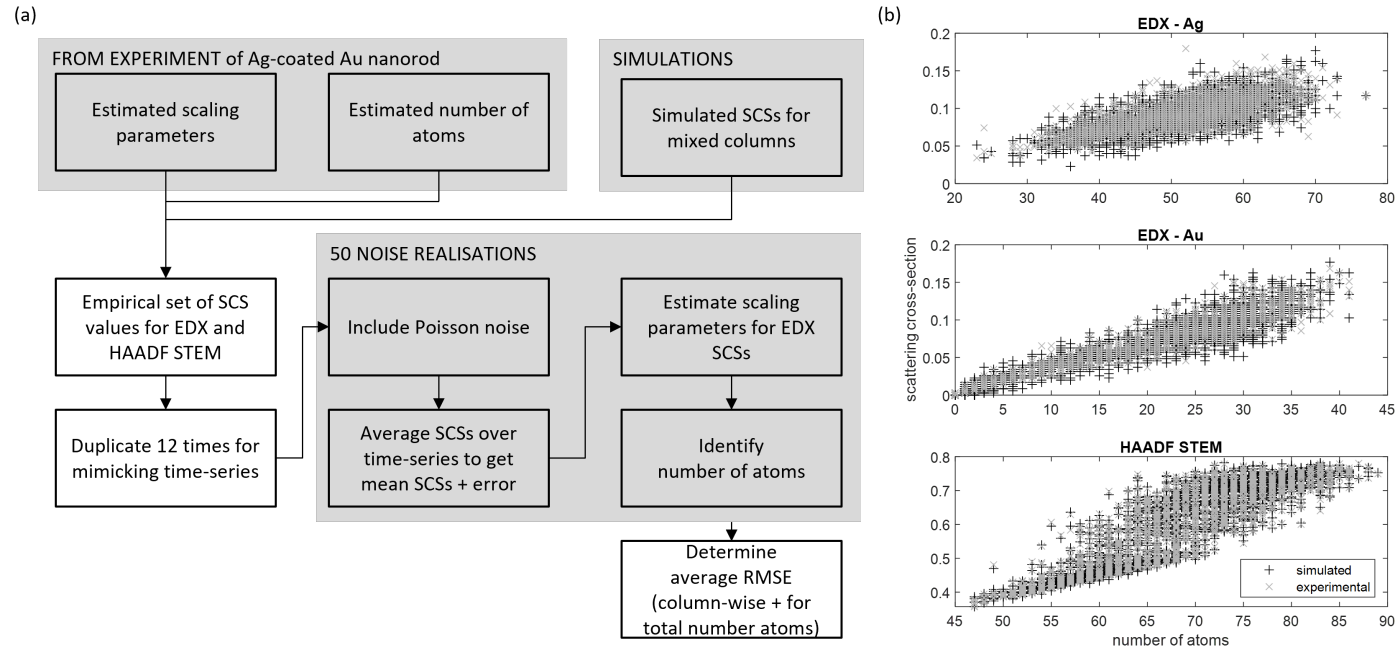

Figure 1: (a) Schematic of the empirical simulation of scattering cross-section values. (b) Example of empirically simulated EDX and HAADF STEM scattering cross-sections compared to the experimentally measured scattering cross-sections as a function of the estimated number of atoms.

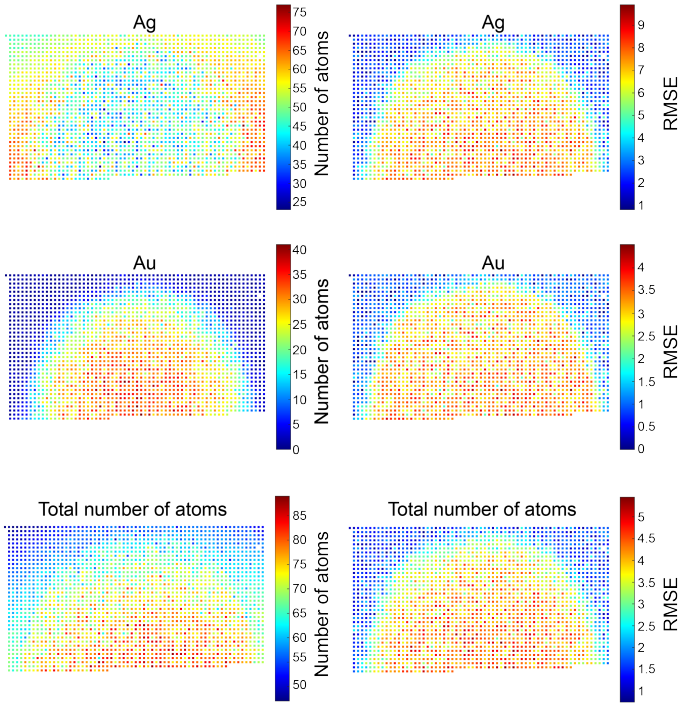

Figure 2: Number of atoms and RMSE for each atomic column for Ag, Au, and the total number of atoms.

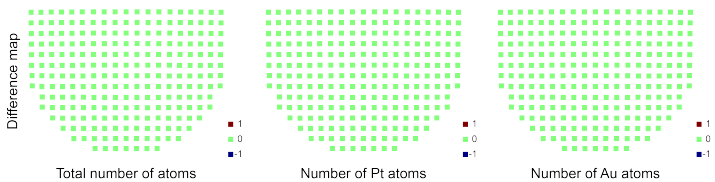

Figure 3: Difference map between the ground truth and estimated atom-counts for the total number of atoms and both the Pt and Au number of atoms in an atomic column for the **unrelaxed** Au@Pt nanorod.

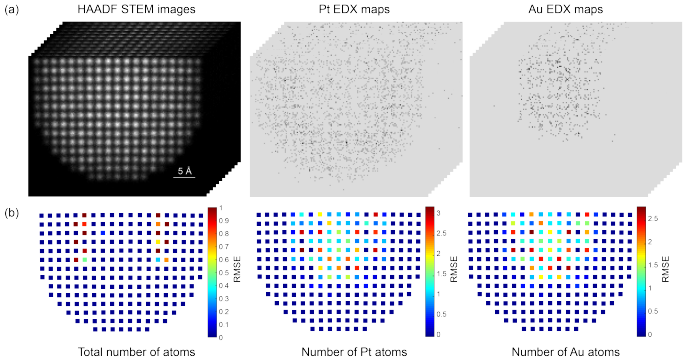

Figure 4: (a) Example of a simulated time-series of HAADF STEM images and Pt and Au elemental maps with 5% collection efficiency. (b) RMSE per atomic column for Pt, Au, and the total number of atoms.